

Extension of the IEEE 39-bus Test Network for the Study of Fundamental Dynamics of Modern Power Systems

Yihui Zuo
Asja Derviškadić
Guglielmo Frigo
Mario Paolone

July, 2019

DISTRIBUTED ELECTRICAL SYSTEMS LABORATORY
ÉCOLE POLYTECHNIQUE FÉDÉRALE DE LAUSANNE, SWITZERLAND

Abstract

This report presents three versions of the dynamic model of the IEEE 39-bus power systems to be used as benchmarks for studying fundamental dynamics of modern power systems in presence of power electronic interfaces. Specifically, the models correspond to three configurations of the IEEE 39-bus power system:

- The original 10-synchronous machine IEEE 39-bus power system;
- An inertia-reduced 39-bus power system, created by replacing 4 synchronous generators with 4 aggregated type-3 wind power plants;
- An inertia-reduced 39-bus power system, created by replacing 4 synchronous generators with 4 aggregated type-3 wind power plants and introducing a Battery Energy Storage System (BESS) connected via a voltage source converter (VSC).

The details of the dynamic models of all the components are thoroughly described. The proposed models, developed to be used on the Opal-RT real-time simulator, are provided in MATLAB/Simulink and are available online¹. Furthermore, this report presents the simulation tests that are conducted with respect to the three configurations, demonstrating the significant influence of inertia reduction on the transient dynamics of power system and the impact of BESS-VSC on power system dynamics.

¹The models are available on Github: <https://github.com/DESL-EPFL/Extension-of-the-IEEE-39-bus-Test-Networkfor-the-Study-of-Fundamental-Dynamics-of-Modern-Power-System.git>

Contents

| | | |
|----------|---|-----------|
| 1 | IEEE 39-Bus Power System Dynamic Model | 6 |
| 1.1 | Synchronous Generators | 8 |
| 1.1.1 | Synchronous machines | 8 |
| 1.1.2 | Turbine-governors | 10 |
| 1.1.3 | Excitation systems | 10 |
| 1.2 | Dynamic Loads | 12 |
| 1.3 | Transmission Lines and Transformers | 13 |
| 1.4 | Wind Power Plants | 15 |
| 1.4.1 | Model of the type-3 DFIG wind turbine | 15 |
| 1.5 | BESS-VSC | 17 |
| 1.5.1 | BESS TTC model | 17 |
| 1.5.2 | Three-level NPC converter | 19 |
| 1.5.3 | VSC grid-feeding control with grid supporting | 21 |
| 2 | Dynamic Simulations | 22 |
| 2.1 | Initial Nodal Power Injections | 22 |
| 2.2 | Simulation Results | 23 |
| A | Model Execution Requirement | 28 |
| A.1 | Software Requirements | 28 |
| A.2 | Hardware Requirements | 28 |

Nomenclature

Synchronous Machine

| | |
|------------|--|
| F | friction factor, Newton per meter per second [$N \cdot m \cdot s$] |
| H | inertia coefficient, second [s] |
| R_s | stator resistance, per-unit [pu] |
| T'_{do} | d-axis transient open-circuit time constant, second [s] |
| T''_{do} | d-axis subtransient open-circuit time constant, second [s] |
| T'_{qo} | q-axis transient open-circuit time constant, second [s] |
| T''_{qo} | q-axis subtransient open-circuit time constant, second [s] |
| X_l | leakage reactance, per-unit [pu] |
| X_d | d-axis synchronous reactance, per-unit [pu] |
| X'_d | d-axis transient reactance, per-unit [pu] |
| X''_d | d-axis subtransient reactance, per-unit [pu] |
| X_q | q-axis synchronous reactance, per-unit [pu] |
| X'_q | q-axis transient reactance, per-unit [pu] |
| X''_q | q-axis subtransient reactance, per-unit [pu] |
| R_p | static droop, percentage [%] |

Hydraulic Turbine and Governor System

| | |
|-------|---|
| K_p | regulator gain |
| K_i | regulator integral gain |
| T_M | mechanical inertia constant, second [s] |
| T_w | water inertia time, second [s] |

Steam Turbine and Governor System

| | |
|-------|---|
| F_2 | turbine torque fraction 2 |
| F_3 | turbine torque fraction 3 |
| F_4 | turbine torque fraction 4 |
| F_5 | turbine torque fraction 5 |
| K_p | regulator gain |
| T_2 | steam turbine time constant 2, second [s] |

| | |
|----------|--|
| T_3 | steam turbine time constant 3, second [s] |
| T_4 | steam turbine time constant 4, second [s] |
| T_5 | steam turbine time constant 5, second [s] |
| T_{sm} | steam turbine servomotor time constant, second [s] |
| T_{sr} | steam turbine speed delay, second [s] |

Synchronous Machine Excitation System

| | |
|-------|---|
| K_a | voltage regulator gain |
| K_f | damping filter gain |
| T_a | voltage regulator time constant, second [s] |
| T_b | transient gain reduction lead time constant, second [s] |
| T_c | transient gain reduction lag time constant, second [s] |
| T_f | damping filter time constant, second [s] |
| T_r | low-pass filter time constant, second [s] |

Wind Power Plant

| | |
|-------------|---|
| C_{dc} | capacitance of DC capacitor for back-to-back converter, farad [F] |
| H | inertia constant of asynchronous machine, second [s] |
| L_{choke} | inductance of AC reactor for back-to-back converter, henry [H] |
| L_m | mutual inductance of asynchronous machine, per-unit [pu] |
| L_r | rotor inductance of asynchronous machine, per-unit [pu] |
| L_r | rotor inductance of asynchronous machine, per-unit [pu] |
| L_s | stator inductance of asynchronous machine, per-unit [pu] |
| R_{choke} | resistance of AC reactor for back-to-back converter, ohm [Ω] |
| R_r | rotor resistance of asynchronous machine, per-unit [pu] |
| R_s | stator resistance of asynchronous machine, per-unit [pu] |

VSC Electrical Elements

| | |
|------------------|--|
| C_{dc} | DC-link capacitance, farad [F] |
| C_{dcf} | capacitance of DC filter, farad [F] |
| f_{T1}, f_{T2} | AC filter tuning frequency, hertz [Hz] |
| L_{dcf} | inductance of DC filter, henry [H] |
| L_r | inductance of AC reactor, henry [H] |
| L_{sr} | inductance of DC smooth reactor, henry [H] |
| Q_{f1}, Q_{f2} | AC filter nominal reactive power, volt-ampere reactive [var] |

R_{dcf} resistance of DC filter, ohm [Ω]
 R_r resistance of AC reactor, ohm [Ω]
 R_{sr} resistance of DC smooth reactor, ohm [Ω]

List of abbreviations

AVR automatic voltage regulator
BESS battery energy storage system
DFIG doubly-fed induction generator
EMTP electromagnetic transmission program
IGBT insulated-gate bipolar transistor
PFR primary frequency regulation
PLL phase locked loop
RMS root mean square
SFR secondary frequency regulation
SOC state of charge
SSM state space model
TTC three-time constant
VSC voltage source converters

1 IEEE 39-Bus Power System Dynamic Model

This section provides all the details of the three proposed 39-bus dynamic models, that correspond to three configurations of the IEEE 39-bus power system:

- **Config. I:** The original 10-synchronous machine system (Fig. 1a);
- **Config. II:** An inertia-reduced system (Fig. 1b), where 4 synchronous generations (i.e. G1, G5, G8, and G9) are replaced by 4 wind plants (i.e. WP1, WP2, WP3 and WP4). The wind plants modeled as aggregated type-3 turbines;
- **Config. III:** An inertia-reduced system with a BESS-VSC (Fig. 1c), including the same wind power plants as in Config. II while integrating a BESS-VSC in bus 17.

The full-replica dynamic models and the corresponding parameters of all the simulated devices are provided in the following Sections. Specifically, we thoroughly describe the details of the adopted synchronous generators, dynamic loads, transmission lines, transformers, wind power plants, battery energy storage system and voltage source converter. It is important to note that we follow the parameters provided in the original EPRI RP744-1 Technical Report [1]. Nevertheless, the dynamic models proposed in our report are more detailed than those originally presented in [1].

In what follows, all the adopted models and the correspondingly required parameters are illustrated, making reference to either IEEE Standards or the current literature.

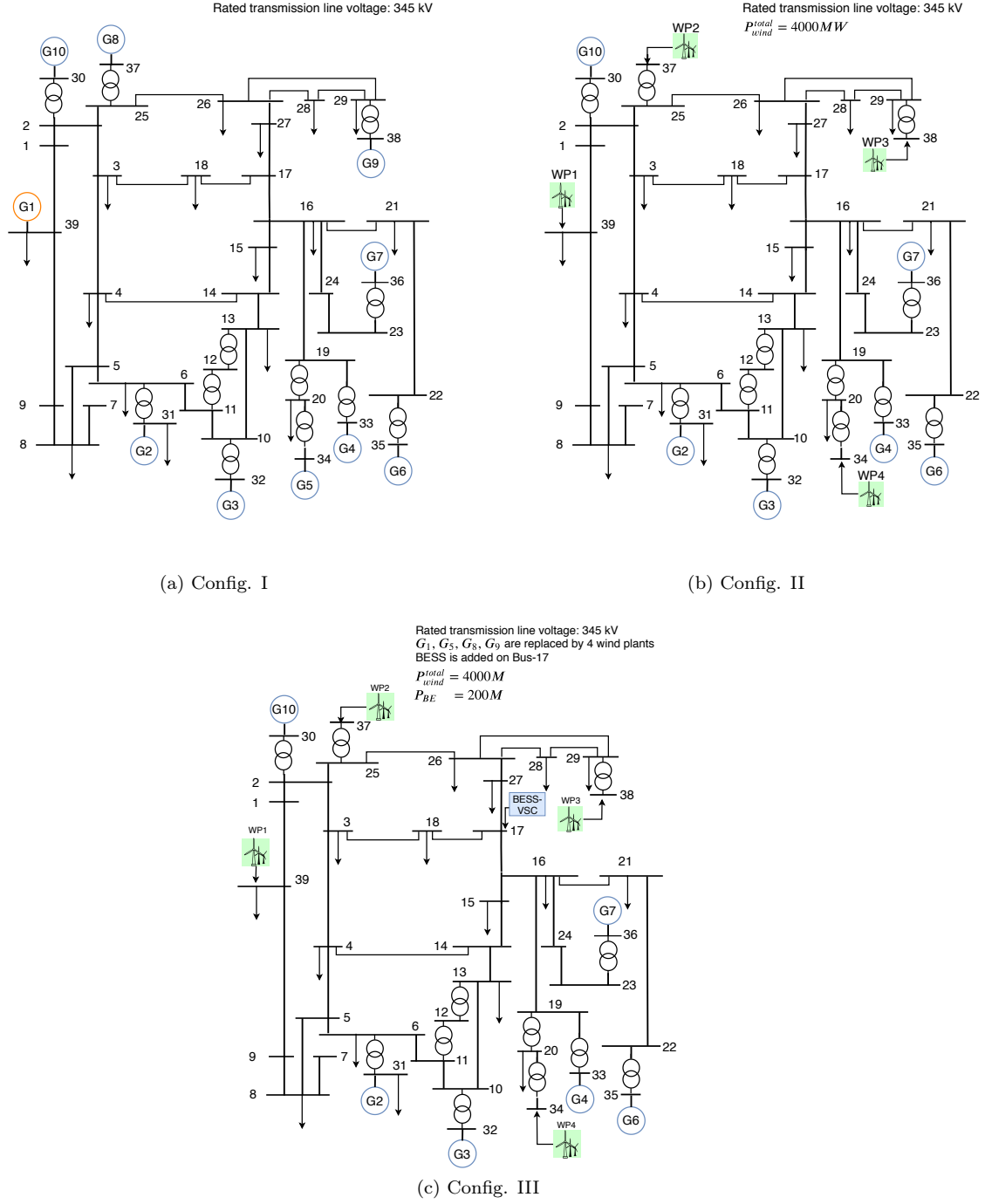


Figure 1: Configurations of the IEEE 39-bus dynamic power system.

1.1 Synchronous Generators

The conventional generation asset of this power grid consists of both hydro- and thermal-power plants. They are simulated by means of a six-order state-space model for the synchronous machine, a prime mover [2], a DC1A excitation system associated with an AVR [3]. The generator model includes a PFR with a static droop coefficient $R_p = 5\%$. The power plant G7 also implements a SFR, whose integration time constant is set equal to 120 s. Table 1 summarizes the types and frequency regulations of the adopted synchronous generators. The parameters for the two-axis model of the synchronous machines, turbine governor and excitation system are shown in Table 5. For each synchronous generator model, the values in per unit are given on their own system base.

Table 1: Synchronous generators summary.

| Generation | Type | Frequency Regulation |
|---------------|---------------|----------------------|
| G1 | Thermal Plant | PFR |
| G2-G6, G8-G10 | Hydro Plant | PFR |
| G7 | Hydro Plant | SFR |

1.1.1 Synchronous machines

The generator model provided in the original technical report is essentially a four-order generator model, as it does not include the subtransient circuits. Therefore, in the current report, we adopt a different model. Specifically, we use a six-order state-space model for the synchronous machine, whose synchronous and transient parameters ($R_s, X_l, X_d, X_q, X'_d, X'_q, T'_{d0}, T'_{q0}$) are taken from the original technical report [1], while the subtransient parameters ($X''_d, X''_q, T''_{d0}, T''_{q0}$) are inspired from real-world test parameters, adapted from the IEEE Std. 1110TM-2002(R2007) [4] and in the EPRI technical reports [5], [6].

In the original report [1], the per unit values are given with respect to the base power of 100 MW. Conversely, in Table 2 we select the base power according to the IEEE Std. 115-1995 [7]:

$$Z_{base} = \frac{E_N^2}{S_N}$$

where E_N is the stator nominal line-to-line voltage and S_N is the three-phase apparent power of the machine.

Table 2: Parameters for synchronous machines.

| Unit | | G1 | G2 | G3 | G4 | G5 | G6 | G7 | G8 | G9 | G10 |
|------------------------|-----------|-------|-------|-------|-------|--------|-------|-------|-------|-------|-------|
| Capacity [MVA] | | 3000 | 1000 | 1000 | 1000 | 520 | 1000 | 1000 | 1000 | 1000 | 1000 |
| Nominal Voltage [kV] | | 22 | 22 | 22 | 22 | 22 | 22 | 22 | 22 | 22 | 22 |
| Synchronous Machine | H [s] | 16.7 | 3.03 | 3.58 | 2.86 | 5.2 | 3.48 | 2.64 | 2.43 | 3.45 | 4.2 |
| | Rs [pu] | 0 | 0 | 0 | 0 | 0 | 0.006 | 0 | 0.001 | 0 | 0 |
| | Xl [pu] | 0.09 | 0.35 | 0.3 | 0.3 | 0.28 | 0.022 | 0.32 | 0.28 | 0.3 | 0.13 |
| | Xd [pu] | 0.6 | 2.95 | 2.5 | 2.62 | 3.48 | 2.54 | 2.95 | 2.90 | 2.1 | 1 |
| | Xq [pu] | 0.57 | 2.82 | 2.37 | 2.58 | 3.224 | 2.41 | 2.62 | 2.80 | 2.05 | 0.69 |
| | X'd [pu] | 0.18 | 0.7 | 0.53 | 0.44 | 0.686 | 0.5 | 0.49 | 0.57 | 0.57 | 0.31 |
| | X'q [pu] | 0.24 | 1.7 | 0.88 | 1.66 | 0.8632 | 0.81 | 1.86 | 0.91 | 0.59 | 0.4 |
| | X''d [pu] | 0.12 | 0.367 | 0.287 | 0.321 | 0.215 | 0.419 | 0.31 | 0.354 | 0.306 | 0.359 |
| | X''q [pu] | 0.12 | 0.359 | 0.33 | 0.411 | 0.213 | 0.471 | 0.403 | 0.228 | 0.306 | 0.383 |
| | T'do [s] | 7 | 6.56 | 5.7 | 5.69 | 5.4 | 7.3 | 5.66 | 6.7 | 4.79 | 10.2 |
| | T'qo [s] | 0.7 | 1.5 | 1.5 | 1.5 | 1.5 | 0.4 | 1.5 | 1.5 | 1.96 | 0.2 |
| | T''do [s] | 0.029 | 0.041 | 0.041 | 0.07 | 0.031 | 0.008 | 0.007 | 0.021 | 0.04 | 0.052 |
| | T''qo [s] | 0.053 | 0.065 | 0.065 | 0.019 | 0.019 | 0.019 | 0.053 | 0.019 | 0.062 | 0.35 |

1.1.2 Turbine-governors

Hydraulic turbine and governor system

We adopt the commonly-used standard hydro turbine governor model as illustrated in [8], [9]. According to [10], the response of the turbine governing system should be tuned to match the rotating inertia, the water column inertia, the turbine control servomotor timing and the characteristics of the connected electrical load. Therefore, as recommended in [10], we use:

$$\begin{aligned} T_M &= 2H \\ T_M : T_w &= 3 : 1 \end{aligned}$$

where, H is the generator inertia constant, T_M is the mechanical inertia constant, and T_w is water inertia time (also known as "water starting time"). The PI governor parameters are derived according to [11]:

$$\begin{aligned} 1/K_P &= 0.625T_w/H \\ K_P/K_I &= 3.33T_w \end{aligned}$$

Accordingly, the parameters for the hydraulic turbine and PI regulator are given in Table 3.

Table 3: Parameters for hydro turbine-governors.

| Unit | Hydraulic Turbine | | PI Regulator | |
|------|-------------------|-----------|--------------|-------|
| | T_M [s] | T_w [s] | K_P | K_I |
| G2 | 6.06 | 2.02 | 2.4 | 0.36 |
| G3 | 7.16 | 2.39 | 2.4 | 0.30 |
| G4 | 5.72 | 1.90 | 2.4 | 0.38 |
| G5 | 10.4 | 3.47 | 2.4 | 0.21 |
| G6 | 6.96 | 2.32 | 2.4 | 0.31 |
| G7 | 5.28 | 1.76 | 2.4 | 0.41 |
| G8 | 4.86 | 1.62 | 2.4 | 0.44 |
| G9 | 6.90 | 2.30 | 2.4 | 0.31 |
| G10 | 8.40 | 2.80 | 2.4 | 0.26 |

Steam turbine and governor system

The steam turbine and governor model are adapted from [2], where the steam turbine system is presented as tandem-compound, single mass model and the speed governor consists of a proportional regulator, a speed delay and a servo motor controlling the gate opening. The parameters for the steam turbine-governor are taken from the typical values used, for instance, in [2], [12].

Table 4: Parameters for steam turbine-governors.

| Unit | Steam Turbine | | | | | | | | Speed Governor | | |
|------|---------------|--------|--------|--------|----|------|------|------|----------------|--------------|--------------|
| | T2 [s] | T3 [s] | T4 [s] | T5 [s] | F2 | F3 | F4 | F5 | K_p | T_{sr} [s] | T_{sm} [s] |
| G1 | 0 | 0.5 | 7 | 0.3 | 0 | 0.36 | 0.36 | 0.28 | 1 | 0.1 | 0.3 |

1.1.3 Excitation systems

The excitation system implements the IEEE DC type 1 exciter associated with an AVR [3]. The parameters are adapted from [13] and are provided in Table 5.

Table 5: Parameters for excitation systems.

| Unit | | G1 | G2 | G3 | G4 | G5 | G6 | G7 | G8 | G9 | G10 |
|---------|-----------|-------|-------|-------|-------|-------|-------|-------|-------|-------|-------|
| Exciter | T_r [s] | 0.01 | 0.01 | 0.01 | 0.01 | 0.01 | 0.01 | 0.01 | 0.01 | 0.01 | 0.01 |
| | K_a | 200 | 200 | 200 | 200 | 200 | 200 | 200 | 200 | 200 | 200 |
| | T_a [s] | 0.015 | 0.015 | 0.015 | 0.015 | 0.015 | 0.015 | 0.015 | 0.015 | 0.015 | 0.015 |
| | T_b [s] | 10 | 10 | 10 | 10 | 10 | 10 | 10 | 10 | 10 | 10 |
| | T_c [s] | 1 | 1 | 1 | 1 | 1 | 1 | 1 | 1 | 1 | 1 |
| | K_f | 0.001 | 0.001 | 0.001 | 0.001 | 0.001 | 0.001 | 0.001 | 0.001 | 0.001 | 0.001 |
| | T_f [s] | 0.1 | 0.1 | 0.1 | 0.1 | 0.1 | 0.1 | 0.1 | 0.1 | 0.1 | 0.1 |

1.2 Dynamic Loads

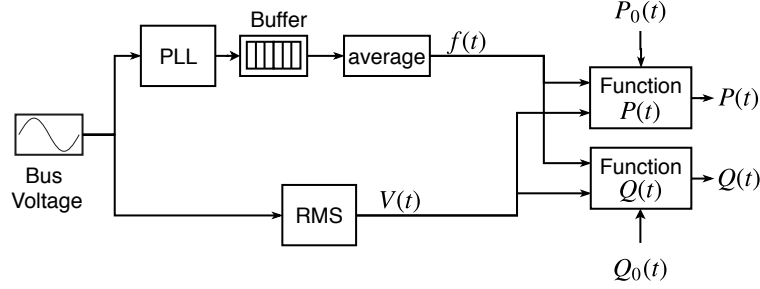


Figure 2: Diagram of the EPRI LOADSYN dynamic load model.

In order to reproduce a plausible dynamic load behavior, the EPRI LOADSYN model has been used [14]. Specifically, the load response to voltage and frequency variations is modeled according to the following time-domain functions:

$$P(t) = P_0(t) \left(\frac{V(t)}{V_0} \right)^{K_{pv}} [1 + K_{pf}(f(t) - f_0)]$$

$$Q(t) = Q_0(t) \left(\frac{V(t)}{V_0} \right)^{K_{qv}} [1 + K_{qf}(f(t) - f_0)]$$

where $P(t)$ and $Q(t)$ are the total three-phase load active and reactive power. The parameters K_{pv} , K_{pf} , K_{qv} , K_{qf} are obtained from typical load voltage and frequency parameters inferred from EPRI LOADSYN program [14]. In this regard, we represent $f(t)$, $V(t)$, $P_0(t)$, and $Q_0(t)$ as time-varying variables sampled with a resolution of 20 ms. The voltage waveform used to feed the dynamic load model is the one at phase "a". We assume that $P_0(t)$ and $Q_0(t)$ are active and reactive power profiles at the rated frequency and voltage (i.e., 50 Hz and 345 kV). These demand profiles are derived from a monitoring system based on PMUs installed on the 125 kV sub-transmission system of the city of Lausanne, Switzerland [15]. Coherently with the other model variables, the measured time-series power data are sampled with a resolution of 20 ms. Since the nominal load values in the original IEEE 39-Bus power system are different from our measured data, the implemented time series used to produce $P_0(t)$ and $Q_0(t)$ are obtained by re-scaling the measured time series.

The implementation of the EPRI LOADSYN model is illustrated in Fig. 2. A PLL and a RMS operator measure the bus frequency and voltage feeding the dynamic load model. In order to smooth the response of the PLL in transient conditions, a moving average operator is implemented.

Specifically, the PLL-tracked frequency is updated every 1 ms, and then buffered for averaging. The overall buffer size is 240 samples, with an overlap size of 220 samples (i.e., the final frequency $f(t)$ is reported every 20 ms). On the other side, the bus voltage $V(t)$ is given by a RMS operator reporting every 20 ms. The RMS value is computed over a window length of 240 ms, as to be consistent with the frequency estimation.

1.3 Transmission Lines and Transformers

The transmission line model is a ARTEMiS distributed parameter line with lumped losses [16]. The model is based on Bergeron's travelling wave method used by EMTP-RV [17]. The ARTEMiS distributed parameters line block is optimized for discrete real-time simulation and allows network decoupling. In Table 6, the positive and zero-sequence resistance (R_1 , R_0), inductance (L_1 , L_0) and capacitance (C_1 , C_0) are reported in per length (i.e. Ω/km , H/km , and F/km).

Table 6: Parameters for transmission lines.

| | | Line Data | | | | | | |
|----------|--------|-------------|--------------|--------|--------------|--------|-------------------|--------|
| From Bus | To Bus | Length [km] | R_1 [Ω/km] | R_0 | L_1 [H/km] | L_0 | C_1 [F/km] | C_0 |
| 1 | 2 | 134 | 0.0311 | 0.1243 | 0.0010 | 0.0029 | 1.164 | 0.5280 |
| 1 | 39 | 105 | 0.0113 | 0.0453 | 0.0008 | 0.0023 | 1.590 | 0.7240 |
| 2 | 3 | 49 | 0.0316 | 0.1263 | 0.0010 | 0.0029 | 1.169 | 0.5330 |
| 2 | 25 | 28 | 0.2975 | 1.1893 | 0.0010 | 0.0029 | 1.161 | 0.5290 |
| 3 | 4 | 53 | 0.0292 | 0.1166 | 0.0013 | 0.0039 | 0.9302 | 0.4266 |
| 3 | 18 | 42 | 0.0312 | 0.1247 | 0.0010 | 0.0030 | 1.133 | 0.5170 |
| 4 | 5 | 32.5 | 0.0293 | 0.1172 | 0.0012 | 0.0037 | 0.9200 | 0.4185 |
| 4 | 14 | 33 | 0.0288 | 0.1154 | 0.0012 | 0.0037 | 0.9333 | 0.4242 |
| 5 | 6 | 14 | 0.0340 | 0.1360 | 0.0010 | 0.0029 | 1.157 | 0.5290 |
| 5 | 8 | 32 | 0.0297 | 0.1190 | 0.0011 | 0.0033 | 1.028 | 0.4690 |
| 6 | 7 | 25.5 | 0.0280 | 0.1120 | 0.0011 | 0.0034 | 0.9882 | 0.4471 |
| 6 | 11 | 26.5 | 0.0314 | 0.1258 | 0.0010 | 0.0029 | 1.170 | 0.5320 |
| 7 | 8 | 15 | 0.0317 | 0.1269 | 0.0010 | 0.0029 | 1.160 | 0.5270 |
| 8 | 9 | 93 | 0.0294 | 0.1177 | 0.0012 | 0.0037 | 0.9118 | 0.4140 |
| 9 | 39 | 136 | 0.0087 | 0.0350 | 0.0006 | 0.0017 | 1.966 | 0.8940 |
| 10 | 11 | 14 | 0.0340 | 0.1360 | 0.0010 | 0.0029 | 1.157 | 0.5290 |
| 10 | 13 | 14 | 0.0340 | 0.1360 | 0.0010 | 0.0029 | 1.157 | 0.5290 |
| 13 | 14 | 32 | 0.0335 | 0.1339 | 0.0010 | 0.0030 | 1.200 | 0.5470 |
| 14 | 15 | 70 | 0.0306 | 0.1224 | 0.0010 | 0.0029 | 1.166 | 0.5300 |
| 15 | 16 | 31.5 | 0.0340 | 0.1360 | 0.0010 | 0.0028 | 1.210 | 0.5490 |
| 16 | 17 | 26 | 0.0320 | 0.1281 | 0.0011 | 0.0032 | 1.150 | 0.5230 |
| 16 | 19 | 61 | 0.0321 | 0.1249 | 0.0010 | 0.0030 | 1.110 | 0.5050 |
| 16 | 21 | 46 | 0.0207 | 0.0828 | 0.0009 | 0.0028 | 1.235 | 0.5610 |
| 16 | 24 | 15 | 0.0238 | 0.0952 | 0.0013 | 0.0037 | 1.013 | 0.4600 |
| 21 | 22 | 47 | 0.0203 | 0.0810 | 0.0090 | 0.0028 | 1.217 | 0.5530 |
| 22 | 23 | 33 | 0.0216 | 0.0866 | 0.0009 | 0.0028 | 1.245 | 0.5670 |
| 23 | 24 | 88 | 0.0298 | 0.1190 | 0.0013 | 0.0038 | 0.9148 | 0.4148 |
| 25 | 26 | 101 | 0.0377 | 0.1508 | 0.0010 | 0.0030 | 1.132 | 0.5150 |
| 26 | 27 | 46.5 | 0.0358 | 0.1433 | 0.0010 | 0.0030 | 1.148 | 0.5230 |
| 26 | 28 | 151 | 0.0339 | 0.1356 | 0.0010 | 0.0030 | 1.152 | 0.5240 |
| 26 | 29 | 200 | 0.0339 | 0.1357 | 0.0010 | 0.0030 | 1.146 | 0.5220 |
| 28 | 29 | 48 | 0.0347 | 0.1389 | 0.0010 | 0.0030 | 1.156 | 0.5250 |
| | | | | | | | *10 ⁻⁸ | |

The three-phase transformers are modeled via suitably-connected single-phase transformers, which take into account the winding resistance (R_1 , R_2) and leakage inductance (L_1 , L_2), as well as the magnetization

characteristics of the core, modeled by a linear (Rm , Lm) branch. As shown in Table 7, in Configuration II and III, when replacing 4 synchronous generations with 4 wind plants, the corresponding transformers are modified accordingly. The Table reports the values in per unit with respect to each transformer's base power.

Table 7: Parameters for transformers.

| | | Transformer | | | | | | | |
|----------|--------|-------------|---------------|------------|------------|------------|------------|-----------|-----------|
| From Bus | To Bus | Connection | Capacity [MW] | R_1 [pu] | R_2 [pu] | L_1 [pu] | L_2 [pu] | Rm [pu] | Lm [pu] |
| 2 | 30 | Dy11 | 1419 | 0 | 0 | 0.1284 | 0.1284 | 500 | 500 |
| 6 | 31 | Dy11 | 1000 | 0 | 0 | 0.125 | 0.125 | 500 | 500 |
| 10 | 32 | Dy11 | 1000 | 0 | 0 | 0.1 | 0.1 | 500 | 500 |
| 12 | 11 | Dy11 | 110 | 0.0009 | 0.0009 | 0.0239 | 0.0239 | 500 | 500 |
| 12 | 13 | Dy11 | 110 | 0.0009 | 0.0009 | 0.0239 | 0.0239 | 500 | 500 |
| 19 | 20 | Dy11 | 880 | 0.0031 | 0.0031 | 0.0607 | 0.0607 | 500 | 500 |
| 19 | 33 | Dy11 | 1000 | 0.0350 | 0.0350 | 0.0710 | 0.0710 | 500 | 500 |
| 20 | 34 | Dy11 | 572 | 0.0257 | 0.0257 | 0.0515 | 0.0515 | 500 | 500 |
| 20 | WP4 | Dy11 | 750 | 0 | 0 | 0.0570 | 0.0750 | 500 | 500 |
| 22 | 35 | Dy11 | 1000 | 0 | 0 | 0.0715 | 0.0715 | 500 | 500 |
| 23 | 36 | Dy11 | 1000 | 0.0025 | 0.0025 | 0.1360 | 0.1360 | 500 | 500 |
| 25 | 37 | Dy11 | 1000 | 0.0030 | 0.0030 | 0.1160 | 0.1160 | 500 | 500 |
| 25 | WP2 | Dy11 | 1200 | 30 | 30 | 0.1160 | 0.1160 | 500 | 500 |
| 29 | 38 | Dy11 | 935 | 0.0037 | 0.0037 | 0.0729 | 0.0729 | 500 | 500 |
| 29 | WP3 | Dy11 | 1000 | 0 | 0 | 0.1000 | 0.1000 | 500 | 500 |
| 39 | 39G | Dy11 | 3000 | 0 | 0 | 0.3 | 0.3 | 500 | 500 |
| 39 | WP1 | Dy11 | 2000 | 0 | 0 | 0.1800 | 0.1800 | 500 | 500 |

1.4 Wind Power Plants

1.4.1 Model of the type-3 DFIG wind turbine

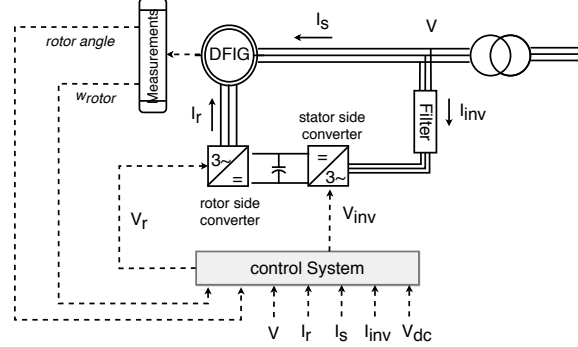


Figure 3: Diagram of the wind plant's model.

The wind power plants are modeled as proposed in [18]. In particular, the power output is approximated by multiplying the power output of a detailed model of a single wind turbine to match the total nominal capacity of the whole wind farm. The diagram of the overall system is shown in Fig. 3.

The model of each wind generator consists of a DFIG and an averaged back-to-back converter model, adapted from [19]. The detailed aerodynamic model of the wind turbine is neglected as the available data directly refers to power inputs into the DFIG provided by the wind turbine. The wind power profiles are generated at 1 second resolution by re-sampling the measurements at 1 minute resolution from ERCOT [20]. The re-sampling approach is based on iterated smoothing and differentiating operations that use the statistical characteristics of the aggregated wind generation profiles presented in [21]. More details about producing wind power profiles are described in [22].

The back-to-back IGBT VSCs are modelled by equivalent voltage sources, which generate the AC voltage averaged over one cycle of the switching frequency. In this averaged converter model, the dynamics resulting from the interaction between the control system and the power system are preserved. Two grid-feeding controls are implemented in the back-to-back converters, as shown in Fig. 4.

Details of the 4 wind power plants are give in Table 8, including the locations, generation capacities and parameters for the asynchronous machines and back-to-back converters. For each asynchronous machine, the parameters in per unit are given with respect to their own system base.

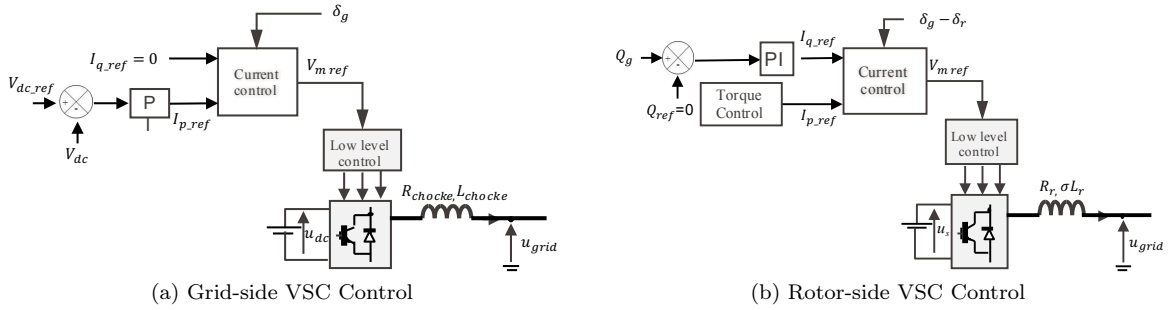


Figure 4: Diagrams of back-to-back converter controllers used in the type-3 wind turbine model.

Table 8: Parameters of the wind plants.

| Unit | Type | Bus | Capacity [MW] | Asynchronous Machine [pu] | | | | | | Back-to-back Converter | | |
|------|--------|-----|------------------|---------------------------|----------------|----------------|----------------|----------------|-------|------------------------|--------------------|------------------------|
| | | | | R _s | L _s | R _r | L _r | L _m | H [s] | R_{choke} [Ω] | L_{choke} [H] | C _{dc} [F] |
| WP1 | Type-3 | 39 | 1600 | 0.00706 | 0.171 | 0.005 | 0.156 | 2.9 | 5.04 | 0.1785 | 0.0568 | 12 |
| WP2 | Type-3 | 37 | 1300 | 0.00706 | 0.171 | 0.005 | 0.156 | 2.9 | 5.04 | 0.2381 | 0.0758 | 9 |
| WP3 | Type-3 | 38 | 900 | 0.00706 | 0.171 | 0.005 | 0.156 | 2.9 | 5.04 | 0.3571 | 0.1137 | 6 |
| WP4 | Type-3 | 34 | 700 | 0.00706 | 0.171 | 0.005 | 0.156 | 2.9 | 5.04 | 0.4285 | 0.1364 | 5 |

1.5 BESS-VSC

Figure 5 presents a simplified diagram of BESS-VSC. Parameters for electrical elements at AC and DC side of the converter are listed in Table. 9. Furthermore, the BESS TTC model, the three-level converter model and the adopted controller are detailed in the sections below.

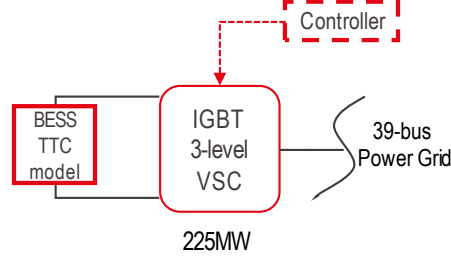


Figure 5: Diagram of BESS-VSC.

Table 9: Parameters for electrical elements at AC and DC side.

| Unit | Capacity [MW] | DC | | | | | | AC | | | | | |
|------|------------------|------------------|------------------|-------------------|------------------|-------------------|-----------------|---------------|---------------|------------------------------|-------------------------------|--|--|
| | | R_{sr} [mΩ] | L_{sr} [mH] | R_{dcf} [mΩ] | C_{dcf} [F] | L_{dcf} [mH] | C_{dc} [F] | R_r [mΩ] | L_r [mH] | $[f_{T1} \ f_{T2}]$ [kHz] | $[Q_{f1} \ Q_{f2}]$ [Mvar] | | |
| VSC | 225 | 0.0013 | 0.004 | 0.0737 | 0.24 | 0.0023 | 1.4 | 0.375 | 0.0009 | [1.35 2.7] | [18 22] | | |

1.5.1 BESS TTC model

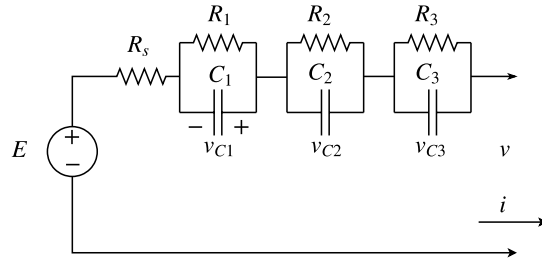


Figure 6: Three Time Constant equivalent circuit.

Figure 6 shows the equivalent circuit of a TTC model, which can be implemented into Simulink as a SSM:

$$\begin{aligned} \frac{dx(t)}{dt} &= A_c(SOC)x(t) + B_c(SOC)u(t) \\ y(t) &= C_c(SOC)x(t) + D_c(SOC)u(t) \end{aligned}$$

$$\text{where, } A_c = \begin{bmatrix} -\frac{1}{R_1 C_1} & 0 & 0 \\ 0 & -\frac{1}{R_2 C_2} & 0 \\ 0 & 0 & -\frac{1}{R_3 C_3} \end{bmatrix}, B_c = \begin{bmatrix} \frac{1}{C_1} & 0 \\ \frac{1}{C_2} & 0 \\ \frac{1}{C_3} & 0 \end{bmatrix}, C_c = [1 \ 1 \ 1], D_c = [R_s \ E],$$

$$x = [v_{C1} \ v_{C2} \ v_{C3}], u(t) = [i_t \ 1].$$

The adopted BESS model (noted as $BESS_{rts}$) is developed on the basis of a TTC model whose parameters have been identified using real data from a 720kW/560kWh BESS (noted as $BESS_{desl}$) available at EPFL-DESL [23]. The electrochemistry of the battery is based on Lithium Titanate Oxide technology. The nominal active power of $BESS_{desl}$ is 720 kW and the nominal DC voltage of the connected inverter is 750 V. The identified SSM parameters are shown in Table 10.

Table 10: Parameters of 560 kWh Lithium Titanate Oxide BESS available at EPFL-DESL.

| SOC [%] | 0-20 | 20-40 | 40-60 | 60-80 | 80-100 |
|---------|--------|--------|--------|--------|--------|
| E | 592.2 | 625.0 | 652.9 | 680.2 | 733.2 |
| Rs | 0.029 | 0.021 | 0.015 | 0.014 | 0.013 |
| R1 | 0.095 | 0.075 | 0.090 | 0.079 | 0.199 |
| C1 | 8930 | 9809 | 13996 | 12000 | 11234 |
| R2 | 0.04 | 0.009 | 0.009 | 0.009 | 0.10 |
| C2 | 909 | 2139 | 2482 | 2490 | 2505 |
| R3 | 2.5e-3 | 4.9e-5 | 2.4e-4 | 6.8e-4 | 6.0e-4 |
| C3 | 544.2 | 789.0 | 2959.7 | 4500 | 6177.3 |

Since the nominal active power of the $BESS_{desl}$ is way lower than the one to be connected to a HV transmission grid, the $BESS_{desl}$ SSM (noted as SSM_{desl}) has to be scaled-up to obtain a 200 MW $BESS_{rts}$ SSM (noted as SSM_{rts}). To this end, the SSM_{rts} is obtained by connecting in parallel 156 battery packs, where each battery pack consists of two SSM_{desl} connected in series. Figure 7 shows the configuration of the SSM_{rts} . Details about the SSM_{rts} are given here below.

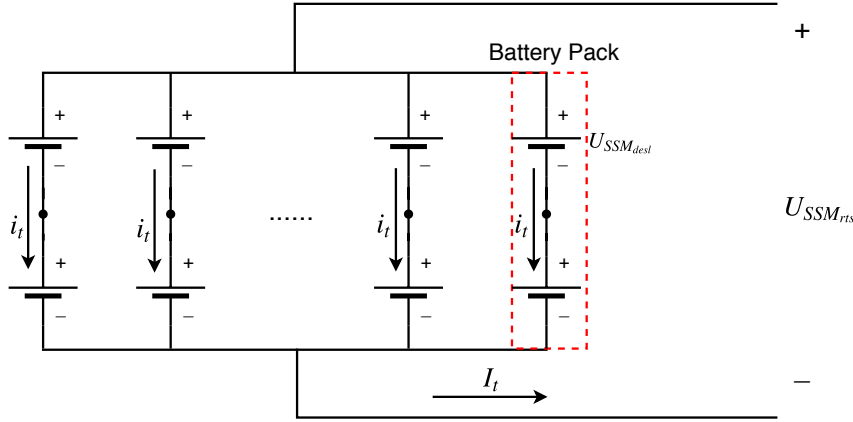


Figure 7: Configuration of SSM_{rts} .

As one battery pack is formed by two 720kW/560kWh BESSs connected in series (refer to the red rectangle in Fig. 7), the total nominal power capacity and energy capacity of the battery pack become 1.44 MW and 1.12 MWh, respectively. Accordingly, the nominal DC voltage of the connected inverter is doubled to 1.5 kV. The modeled $BESS_{rts}$ consists of 156 battery packs connected in parallel, therefore, the total nominal power capacity and energy capacity become 225 MW and 176 MWh, respectively.

Assuming that all paralleled battery packs are identical, the voltage of each battery pack is equal to the voltage of $BESS_{rts}$. Consequently, the parameters for SSM_{rts} are obtained as shown in Table 11. Thereby,

the SSM_{rts} is formulated as:

$$\begin{aligned}\frac{dx^*(t)}{dt} &= A_c^*(SOC)x^*(t) + B_c^*(SOC)u^*(t) \\ y^*(t) &= C_c^*(SOC)x^*(t) + D_c^*(SOC)u^*(t)\end{aligned}$$

where, $A_c^* = \begin{bmatrix} -\frac{1}{R_1 C_1} & 0 & 0 \\ 0 & -\frac{1}{R_2 C_2} & 0 \\ 0 & 0 & -\frac{1}{R_3 C_3} \end{bmatrix}$, $B_c^* = \begin{bmatrix} \frac{1}{C_1} & 0 \\ \frac{1}{C_2} & 0 \\ \frac{1}{C_3} & 0 \end{bmatrix}$, $C_c^* = [1 \ 1 \ 1]$, $D_c^* = [R_s^* \ E^*]$, $x^* = [v_{C1} \ v_{C2} \ v_{C3}]$, $u^*(t) = [\frac{I_t}{156} \ 1]$, and $U_{SSM_{rts}} = y^*(t)$. It is worth pointing out that the input current of the SSM_{rts} (first input of the vector $u^*(t)$) is $\frac{I_t}{156}$, where I_t is the total DC current absorbed/provided by the $BESS_{rts}$.

Table 11: Parameters of 176 MWh BESS to be connected to HV transmission grid

| SOC [%] | 0-20 | 20-40 | 40-60 | 60-80 | 80-100 |
|---------|--------|--------|--------|---------|---------|
| E^* | 1184.4 | 1250.0 | 1305.8 | 1360.4 | 1466.4 |
| R_s^* | 0.052 | 0.042 | 0.030 | 0.028 | 0.026 |
| $R1^*$ | 0.190 | 0.150 | 0.180 | 0.158 | 0.398 |
| $C1^*$ | 4465 | 4904.5 | 6998 | 6000 | 5617 |
| $R2^*$ | 0.08 | 0.018 | 0.018 | 0.018 | 0.20 |
| $C2^*$ | 454.5 | 1069.5 | 1241 | 1245 | 1252.5 |
| $R3^*$ | 5.0e-3 | 9.8e-5 | 4.8e-4 | 13.6e-4 | 12.0e-4 |
| $C3^*$ | 272.1 | 394.5 | 1479.8 | 2250 | 3088.7 |

Regarding the SOC model, as we assume all the battery packs operating identically, an aggregated $BESS_{rts}$ SOC model is adopted for computing battery SOC according to:

$$SOC_{k+1} = SOC_k + \frac{T_s}{3600} \frac{I_k/156}{C_{nom}}$$

where $C_{nom} = 750$ Ah (ampere-hour) is the BESS capacity denoted in ampere-hour, $T_s = 0.001$ s is the SOC model sampling rate, and I_k is the total DC current absorbed/provided by the $BESS_{rts}$.

1.5.2 Three-level NPC converter

The BESS is integrated into the IEEE 39-bus through an aggregated fully modeled three-level neutral-point clamped (NPC) converter. Figure 8 shows the original Simulink model of the 3-level converter, which can not be directly implemented in the real-time simulation model due to the fact that it involves too many switching devices in one state space nodal (SSN) group [24]. The solution is to distribute those switch devices into different SSN groups as shown in Fig. 9. The three bridge arms (one arm refers to the red rectangle in Fig. 8) of the 3-level converter are respectively included into subsystem "3-level NPC 1", "3-level NPC 2" and "3-level NPC 3". Each arm interface with AC and DC side through two ARTMiS-SSN interface blocks that are used to define nodes and groups of SSN solver.

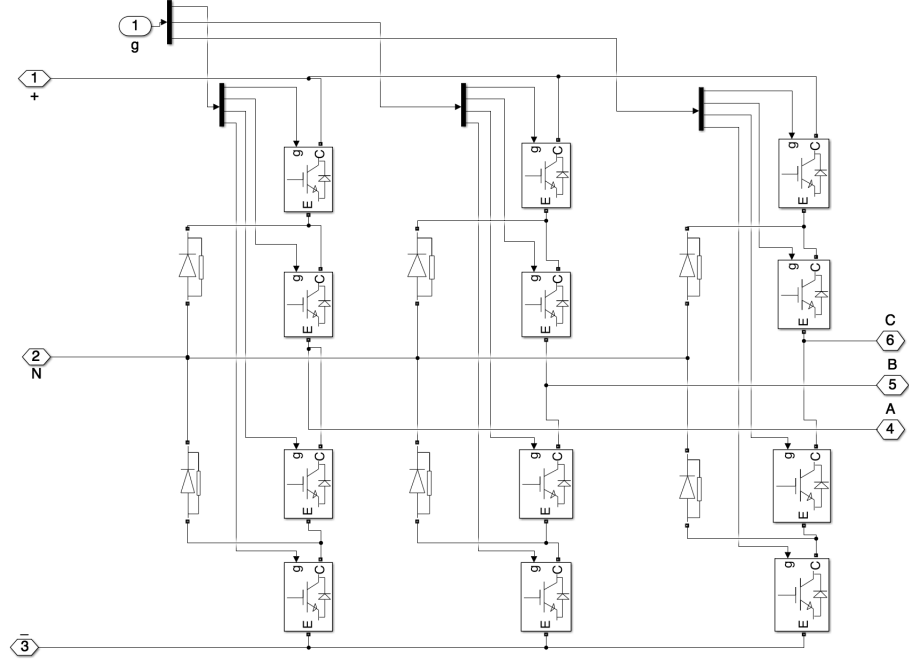


Figure 8: IGBT-based 3-level converter.

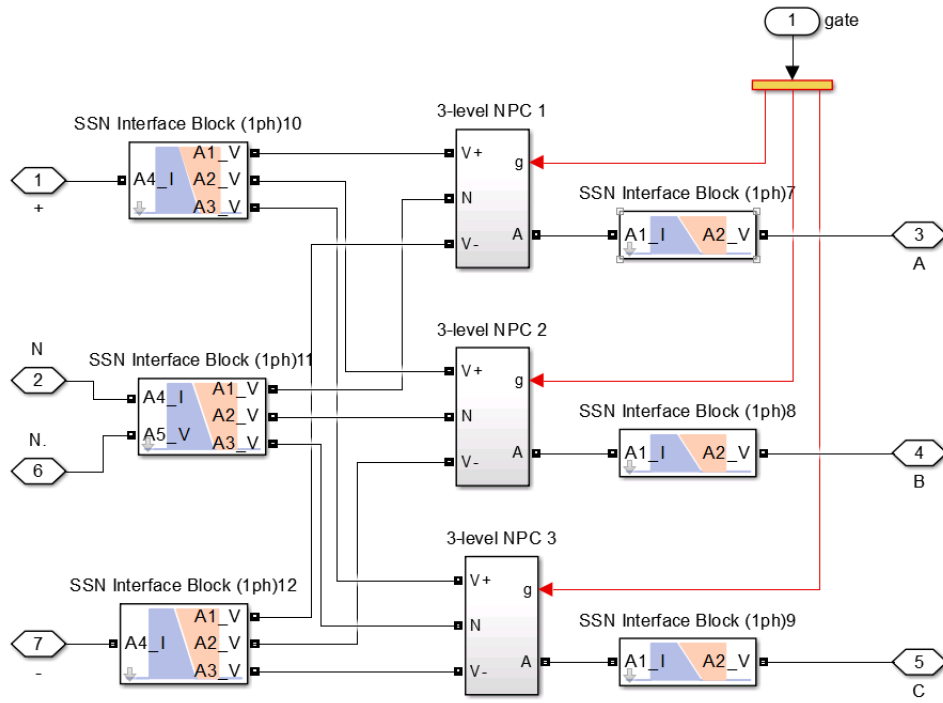


Figure 9: IGBT-based 3-level converter model in RT simulation.

1.5.3 VSC grid-feeding control with grid supporting

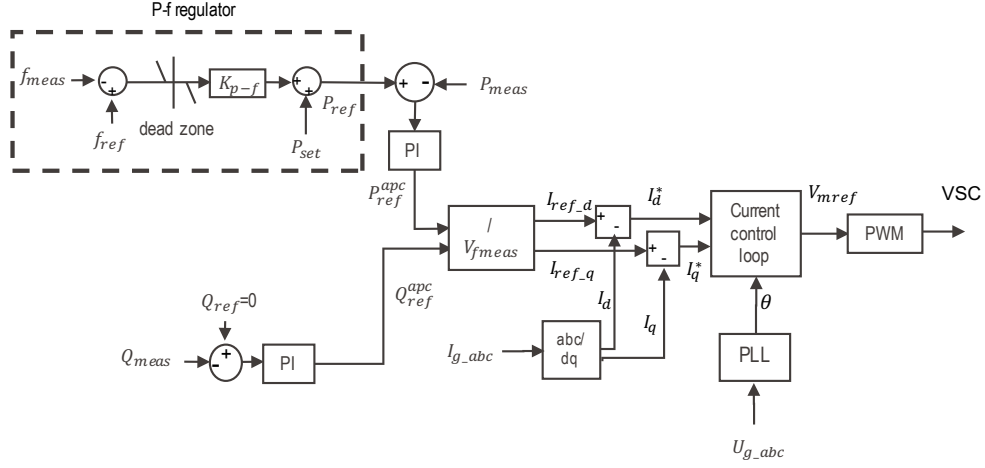


Figure 10: Diagram of the adopted grid-feeding control embedding outer loop control for frequency regulation.

The VSC is implemented with a grid-feeding structure embedding outer control loop that decouples the active and reactive power regulations. As shown in Fig. 10, the active power and reactive power are controlled independently via controlling the direct and quadrature currents. An external frequency regulation control is implemented to provide power grid frequency regulation services. The drop coefficient $K_{p-f} = 20$. It is also worth to mention that the controller limits the maximum/minimum active power to ± 0.95 p.u.

2 Dynamic Simulations

The power network and simulation models are implemented in Matlab Simulink and executed on an OPAL-RT real-time simulator. The advantage is two-fold: (i) it provides a precise quantification of the computational requirements of the simulation, a key element considering the high computational burden due to extended size of the simulated system. (ii) it allows real-time control operation, which enables the test prototyping of multiple time-scales control strategies (e.g. hourly based commitment with minutes-based real-time optimization). The simulation tests conducted for this report use a simulation time step of $25 \mu\text{s}$. Details about software and hardware requirement for executing the real-time simulation model are described in the Appendix A.

This report analyzes three simulations for the corresponding three power system configurations: Config. I, Config. II and Config. III. The same contingency is tested for the three configurations, i.e., the tripping of generator G6 that causes about 800 MW of generation loss. We compare the transient frequency responses in Config. I, Config. II and Config. III during the same contingency.

2.1 Initial Nodal Power Injections

The initial nodal power injections (i.e. power injection before contingency) for the three configurations are listed in Table 12.

Table 12: Initial Nodal Power Injections

| Unit | Active Power [MW] | | | Reactive Power [MVar] | | |
|----------|-------------------|------------|-------------|-----------------------|------------|-------------|
| | Config. I | Config. II | Config. III | Config. I | Config. II | Config. III |
| G1/WF1 | 1311 | 1336 | 1336 | 85 | 85 | 85 |
| G2 | 757 | 572 | 572 | 148 | 56 | 56 |
| G3 | 605 | 489 | 489 | 70 | -61 | -61 |
| G4 | 707 | 543 | 543 | -56 | 13 | 13 |
| G5/WF4 | 411 | 501 | 501 | 65 | 14 | 14 |
| G6 | 807 | 835 | 835 | 118 | 74 | 74 |
| G7 | 467 | 543 | 543 | -22 | -43 | -43 |
| G8/WF2 | 707 | 1145 | 1145 | -107 | 57 | 57 |
| G9/WF3 | 708 | 803 | 803 | -71 | 28 | 28 |
| G10 | 607 | 435 | 435 | 45 | -82 | -82 |
| BESS-VSC | - | - | 0 | - | - | 0 |
| Total | 7087 | 7202 | 7202 | 275 | 141 | 141 |

2.2 Simulation Results

In Fig. 11, we show the generators' rotor speed for the three configurations, as the representation of system frequency dynamics. As it can be seen in the figure, the ROCOF of Config. II and Config. III is significantly larger than in Config. I. Also, the frequency Nadir for Config. II and Config. III is much lower than the one for Config. I. This demonstrates the significant influence of inertia reduction on the transient frequency response of the power systems after the loss of generation.

Moreover, if we compare the rotor speed curves for Config. II with those for Config. III, we can notice that Config. III results in a slower frequency decay and a higher frequency nadir. As shown in the following Fig. 12, that represents the frequency measurements at the wind farms produced by PLLs. Indeed, we can notice that the BESS-VSC in Config. III assists to limit the frequency decreasing velocity and magnitude.

The dynamic performance of the BESS-VSC are specifically shown in Fig. 13. As shown in Fig. 13a and Fig. 13b, during the transient, the implemented external frequency regulator detects the frequency decrease, and accordingly feeds active power to the grid to provide frequency regulation service. It is worth to note that since the maximum active power is limited to 0.95 p.u, the active power holds to 0.95 p.u. even if the frequency keeps decreasing.

Regarding the output reactive power, Fig. 13c shows that the BESS-VSC barely feeds reactive power to the grid. This is due to the fact that we give a constant reactive power reference $Q_{ref} = 0$ to the controller, and the active and reactive power are controlled independently.

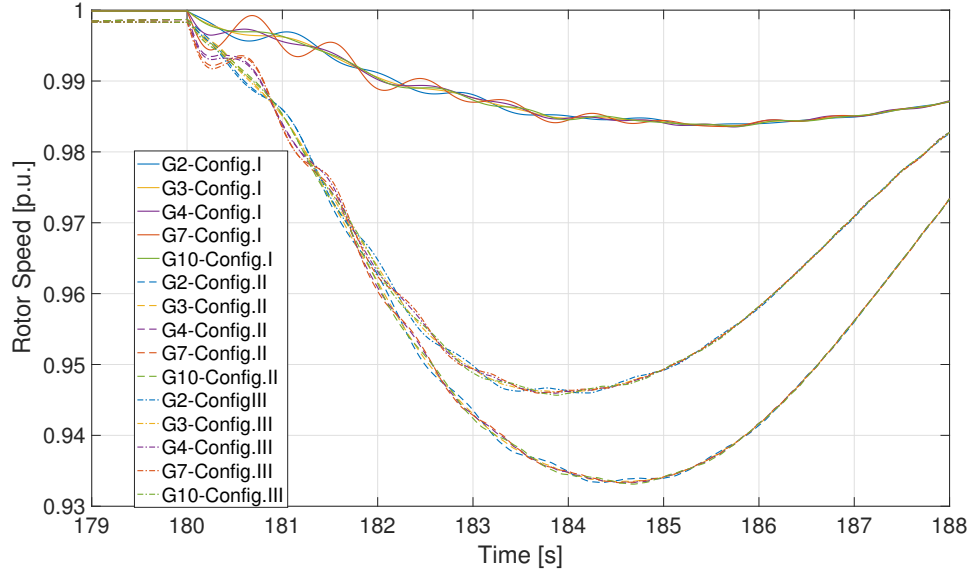


Figure 11: Generators' rotor speed for Config. I, Config. II and Config. III.

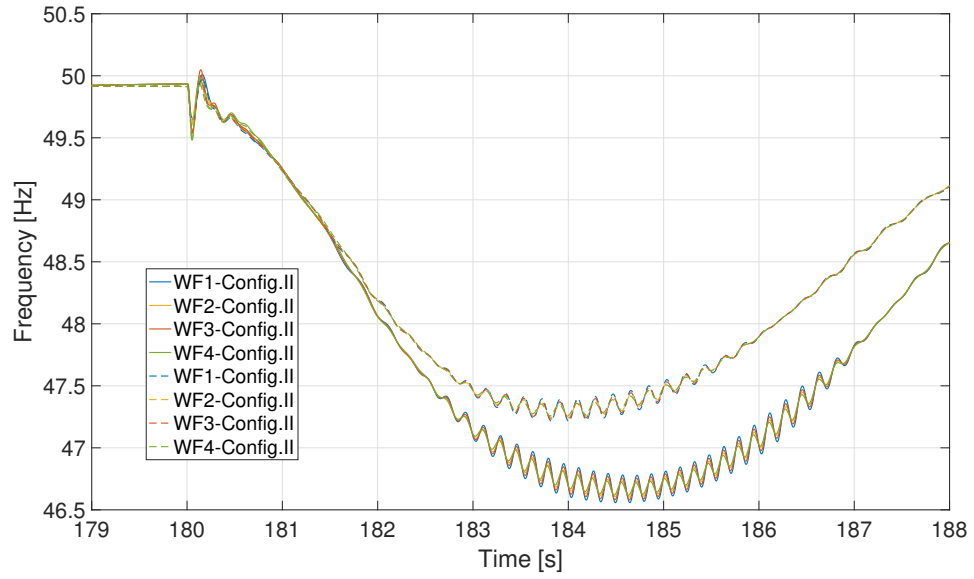
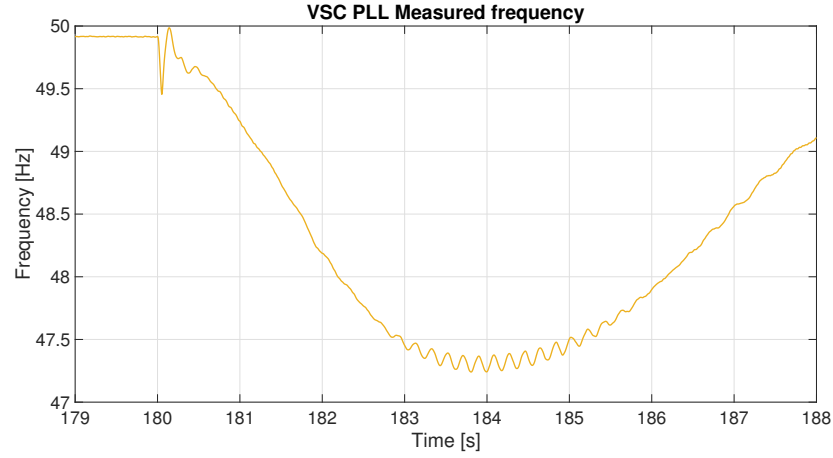
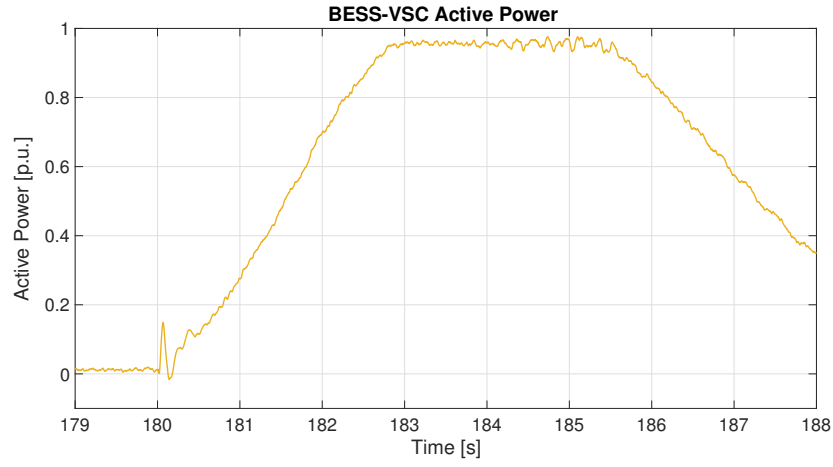


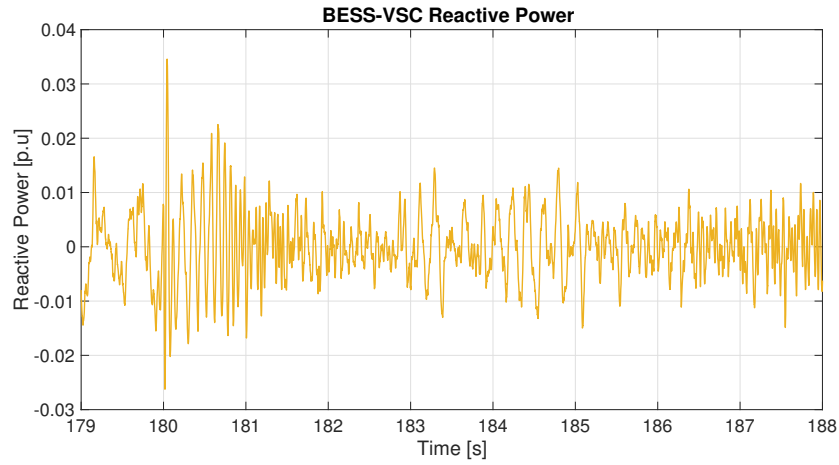
Figure 12: Frequency measurements of wind farms for Config II and Config.III.



(a) BESS-VSC PLL measured frequency.



(b) BESS-VSC active power



(c) BESS-VSC reactive power

Figure 13: BESS-VSC Outputs in Config. III.

References

- [1] R. Byerly, D. Sherman, and R. Bennon, “Phase II: frequency domain analysis of low-frequency oscillations in large electric power systems. Volume 1. Basic concepts, mathematical models, and computing methods.”, Westinghouse Electric Corp., Pittsburgh, PA (USA). Advanced Systems, Tech. Rep., 1982.
- [2] “Dynamic models for steam and hydro turbines in power system studies”, *IEEE Transactions on Power Apparatus and Systems*, no. 6, pp. 1904–1915, 1973.
- [3] “IEEE draft recommended practice for excitation system models for power system stability studies”, *IEEE P421.5/D38, October 2015*, pp. 1–202, Jan. 2015.
- [4] “Ieee guide for synchronous generator modeling practices and applications in power system stability analyses”, *IEEE Std 1110-2002 (Revision of IEEE Std 1110-1991)*, pp. 1–72, 2003.
- [5] “Determination of synchronous machine stability study models. volume 1”, Westinghouse Electric Corp., Pittsburgh, PA (USA). Advanced Systems, Tech. Rep., 1981.
- [6] “Determination of synchronous machine stability study models. volume 2”, Westinghouse Electric Corp., Pittsburgh, PA (USA). Advanced Systems, Tech. Rep., 1981.
- [7] “Ieee guide: Test procedures for synchronous machines”, *IEEE Std 115-1983*, pp. 1–90, Sep. 1983.
- [8] P. Pourbeik *et al.*, “Dynamic models for turbine-governors in power system studies”, *IEEE Task Force on Turbine-Governor Modeling*, no. 2013, 2013.
- [9] J. Feltes, V. Koritarov, L. Guzowski, Y. Kazachkov, B. Lam, C. Grande-Moran, G. Thomann, L. Eng, B. Trouille, P. Donalek, *et al.*, “Review of existing hydroelectric turbine-governor simulation models”, Argonne National Lab.(ANL), Argonne, IL (United States), Tech. Rep., 2013.
- [10] “Ieee guide for the application of turbine governing systems for hydroelectric generating units - redline”, *IEEE Std 1207-2011 (Revision to IEEE Std 1207-2004) - Redline*, pp. 1–139, Jun. 2011.
- [11] “Hydraulic turbine and turbine control models for system dynamic studies”, *IEEE Transactions on Power Systems*, vol. 7, no. 1, pp. 167–179, Feb. 1992.
- [12] P. Kundur, N. J. Balu, and M. G. Lauby, *Power system stability and control*. McGraw-hill New York, 1994, vol. 7.
- [13] I. P. S. D. P. Committee *et al.*, “Power system stability controls subcommittee, benchmark systems for stability controls task force, benchmark systems for small-signal stability analysis and control”, IEEE PES Technical Report PES-TR18, Tech. Rep., 2015.
- [14] “Load representation for dynamic performance analysis (of power systems)”, *IEEE Trans on Pow Sys*, vol. 8, no. 2, pp. 472–482, May 1993.
- [15] A. Derviskadić, P. Romano, M. Pignati, and M. Paolone, “Architecture and experimental validation of a low-latency phasor data concentrator”, *IEEE Trans on Smart Grid*, vol. 9, no. 4, pp. 2885–2893, Jul. 2018.
- [16] Opal-RT technologies Inc, *Rt-lab software, user guide*, English, version Version 8.1, OPAL-RT.
- [17] H. W. Dommel, “Digital computer solution of electromagnetic transients in single-and multiphase networks”, *IEEE Transactions on Power Apparatus and Systems*, vol. PAS-88, no. 4, pp. 388–399, Apr. 1969.
- [18] C. Dufour and J. Belanger, “A real-time simulator for doubly fed induction generator based wind turbine applications”, in *2004 IEEE 35th Annual Power Electronics Specialists Conference*, vol. 5, Jun. 2004, 3597–3603 Vol.5.
- [19] R. Pena, J. C. Clare, and G. M. Asher, “Doubly fed induction generator using back-to-back pwm converters and its application to variable-speed wind-energy generation”, *IEE Proceedings - Electric Power Applications*, vol. 143, no. 3, pp. 231–241, May 1996.
- [20] GE Energy, *Analysis of wind generation impact on ercot ancillary services requirements*, 2008.

- [21] K. Coughlin and J. H. Eto, “Analysis of wind power and load data at multiple time scales”, Lawrence Berkeley National Laboratory (LBNL), Berkeley, CA (United States), Tech. Rep., 2010.
- [22] Y. Zuo, F. Sossan, M. Bozorg, and M. Paolone, “Dispatch and primary frequency control with electrochemical storage: A system-wise verification”, in *2018 IEEE PES Innovative Smart Grid Technologies Conference Europe (ISGT-Europe)*, Oct. 2018, pp. 1–6.
- [23] F. Sossan, E. Namor, R. Cherkaoui, and M. Paolone, “Achieving the dispatchability of distribution feeders through prosumers data driven forecasting and model predictive control of electrochemical storage”, *IEEE Transactions on Sustainable Energy*, vol. 7, no. 4, pp. 1762–1777, Oct. 2016.
- [24] C. Dufour, J. Mahseredjian, and J. Belanger, “A combined state-space nodal method for the simulation of power system transients”, *IEEE Transactions on Power Delivery*, vol. 26, no. 2, pp. 928–935, Apr. 2011.

A Model Execution Requirement

A.1 Software Requirements

MATLAB/Simulink and RT-LAB are required. The models are all built within MATLAB version 8.5.1.281278 (R2015a) Service Pack 1. RT-LAB is a distributed real-time platform that enables the Simulink models to be executed on the OPAL-RT real-time simulators for real-time simulations. The real-time simulations presented in this report are all conducted by RT-LAB version v11.2.2.108 with associated ARTEMIS Blockset version 7.2.2.1206.

Updated MATLAB versions and RT-LAB versions are available and applicable. It is important to check the compatibility between the adopted MATLAB version and RT-LAB version.

A.2 Hardware Requirements

The real-time simulator used for this report is OPAL-RT OP5600 installed with the corresponding RT-LAB version. To execute the published models for real-time simulation, at least 7 cores should be available in the OP5600 simulator. For installation, user guide and more information of the real-time simulator go to: <https://www.opal-rt.com/>.